Volume 24
Number 17
7 May 2022
Pages 9745–10630

PCCP

Physical Chemistry Chemical Physics

rsc.li/pccp

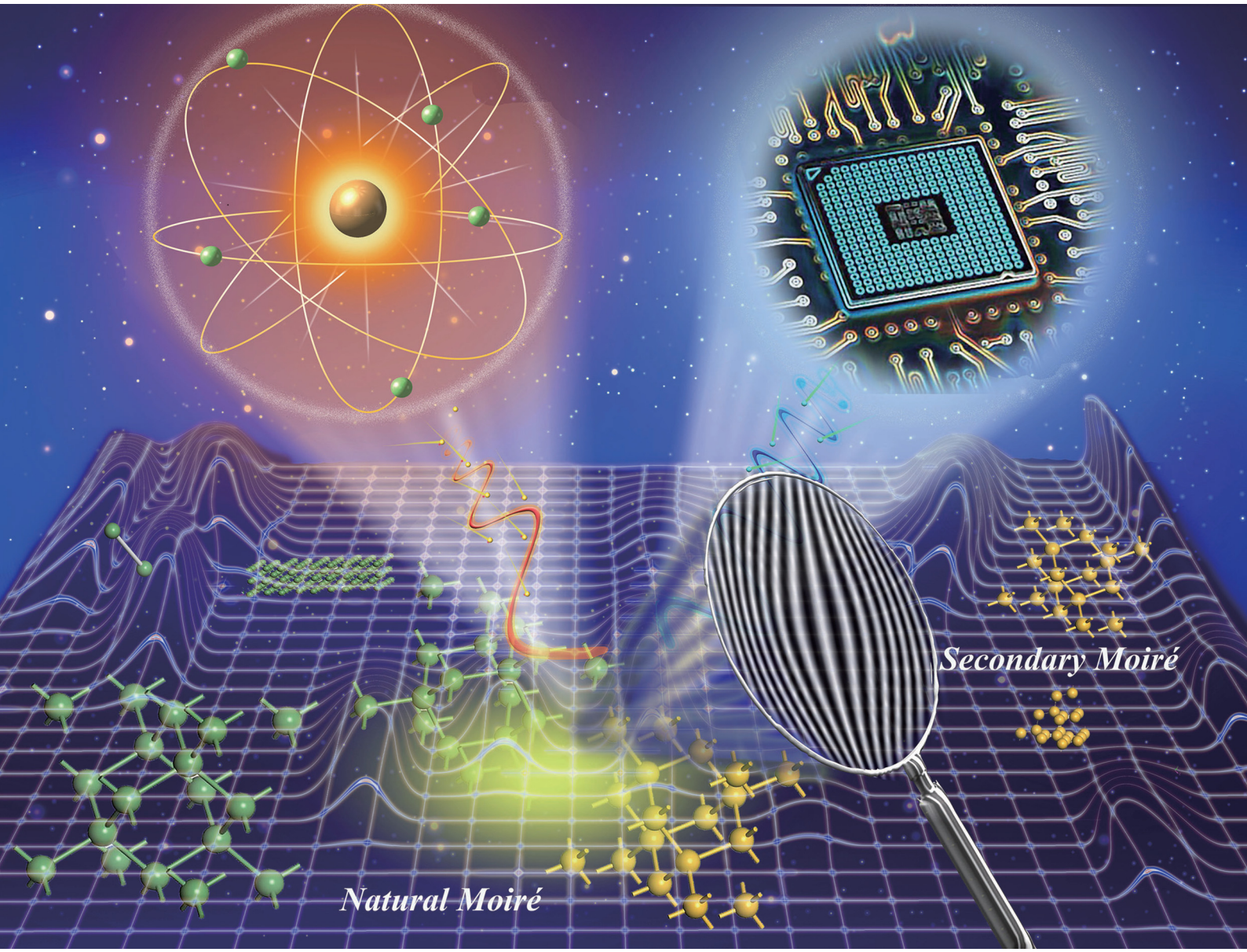

ISSN 1463-9076

ROYAL SOCIETY OF CHEMISTRY

PAPER

Xianfu Huang, Zhanwei Liu *et al.*

Evaluation of interfacial misfit strain field of heterostructures using STEM nano secondary moiré method

PCCP

ROYAL SOCIETY OF CHEMISTRY

PAPER

View Article Online
View Journal | View Issue

Cite this: *Phys. Chem. Chem. Phys.*, 2022, **24**, 9848

Evaluation of interfacial misfit strain field of heterostructures using STEM nano secondary moiré method

Yao Zhao, [a] Yang Yang,[b] Huihui Wen, [c] Chao Liu,[d] Xianfu Huang*[e] and Zhanwei Liu*[a]

Received 24th December 2021,
Accepted 21st February 2022

DOI: 10.1039/d1cp05891f

rsc.li/pccp

STEM nano-moiré can achieve high-precision deformation measurement in a large field of view. In scanning moiré fringe technology, the scanning line and magnification of the existing transmission electron microscope (TEM) cannot be changed continuously. The frequency of the crystal lattice is often difficult to match with the fixed frequency of the scanning line, resulting in mostly too dense fringes that cannot be directly observed; thus, the calculation error is relatively large. This problem exists in both the STEM moiré method and the multiplication moiré method. Herein, we propose the STEM secondary nano-moiré method, *i.e.*, a digital grating of similar frequency is superimposed on or sampling the primary moiré fringe or multiplication moiré to form the secondary moiré. The formation principle of the secondary moiré is analyzed in detail, with deduced theoretical relations for measuring the strain of STEM secondary nano-moiré fringe. The advantages of sampling secondary moiré and digital secondary moiré are compared. The optimal sampling interpolation function is obtained through error analysis. This method expands the application range of the STEM moiré method and has better practicability. Finally, the STEM secondary nano-moiré is used to accurately measure the strain field at the Si/Ge heterostructure interface, and the theoretical strain field calculated by the dislocation model is analyzed and compared. The obtained results are more compatible with the P–N dislocation model. Our work provides a practical method for the accurate evaluation of the interface characteristics of heterostructures, which is an important basis for judging the photoelectric performance of the entire device and the optimal design of the heterostructures.

1. Introduction

Semiconductor heterostructures are generally composed of more than two layers of materials with different parameter lattices, each with a different energy band gap,[1,2] which are produced by molecular beam epitaxy or metal–organic chemical vapor deposition. Due to the mismatch of the crystal lattice at the interface of the two materials, a certain strain is often generated,[3,4] which is sometimes an effective way to design or improve the properties of nanomaterials.[5,6] In addition, the lattice mismatch can also cause dislocations at the interface,[7,8] which will break the symmetry of the crystal structure, change the local bandgap structure,[9] and seriously affect the photoelectric performance of the heterostructure. Therefore, analyzing the strain field of the heterostructure interface is of great significance for improving material properties.[10]

In silicon strain technology and strain engineering, phenomena such as interface mismatch strain and residual strain/stress can be seen everywhere.[11] In recent years, HRTEM (high-resolution transmission electron microscope) has become a powerful tool for measuring the nanometer displacement and strain fields of strained silicon.[12,13] Among them, the geometric phase analysis (GPA) method based on the Fourier space algorithm has been applied to various systems, such as dislocations, nanoparticles, crack tips, and nanoclusters. The scanning nano-moiré method is another good type of measurement method of strain and stress at the nanoscale.[14–16] It is not only like a convex lens that can enlarge the lattice spacing and deformation, but also expands the field of view so that it can be

[a] *School of Aerospace Engineering, Beijing Institute of Technology, Beijing 100081, China. E-mail: liuzw@bit.edu.cn*
[b] *AECC Beijing Institute of Aeronautical Materials, Beijing 100190, China*
[c] *School of Electrical Engineering, Hebei University of Science and Technology, Shijiazhuang 050018, China*
[d] *Key Laboratory of Semiconductor Materials Science, Institute of Semiconductors, Chinese Academy of Sciences, Beijing 100083, China*
[e] *State Key Laboratory of Nonlinear Mechanics (LNM), Institute of Mechanics, Chinese Academy of Sciences, Beijing 100190, China. E-mail: huangxf@imech.ac.cn*

applied to a relatively large area of measurement. However, the existing two-dimensional STEM (scanning transmission electron microscope) moiré technique is limited by the fact that the transmission electron microscope (TEM) cannot continuously change the number of scanning lines and magnification, and the lattice spacing is often difficult to match with the fixed scanning spacing. This leads to the result that most of the fringes obtained by experimental observations are too dense, and large errors occur in the calculation.

In this paper, a STEM secondary nano-moiré method is developed. It is used for large-area, high-precision quantitative analysis of dislocations at the interface of the Si/Ge heterostructure. The strain field in the region is calculated, and the interface stress distribution is quantitatively analyzed combined with elastic theory. The theoretical strain fields calculated by P–N and Foreman dislocation models are compared and discussed. This work provides an important basis for judging the photoelectric performance of the entire device and the optimal design of the heterostructure.

2. Experimental methods

2.1 STEM nano secondary moiré method

STEM nano-moiré may appear when scanning crystalline materials in TEM under certain conditions. This scanning moiré method has the advantages of real-time observation, large field of view, and high sensitivity.[17,18] The strain field of the microdevice can be directly obtained by calculating the moiré fringes. However, due to the limitation of the number of scanning lines and the magnification of TEM, it is usually difficult to match the lattice spacing with the fixed scanning spacing in the existing two-dimensional STEM moiré technology. Here, we developed a STEM secondary nano-moiré method, for which the specific operation steps are as follows.

Fig. 1(a) shows relatively dense moiré fringes at an angle of 5° formed in the vertical direction. Fig. 2(b) shows relatively dense moiré fringes in the vertical direction. If Fig. 1(a) and 2(b) are geometrically superimposed, Fig. 1(c) will be obtained. It can be seen that in addition to the formed secondary moiré, there are also first-order moiré fringes. Further, if the sampling moiré method is applied, the pattern shown in Fig. 1(e) will be formed. The sampling moiré method[19,20] is usually used for the displacement measurement of large infrastructures (such as bridges and buildings). For micro/nano-scale strain distribution measurement, the sampling moiré method has been developed, and several subfamily methods have been successively proposed in the recent years. The reconstructed multiplication moiré method from pixel sampling moiré allows high-sensitivity deformation measurement in a large field of view. Obviously, the fringes in Fig. 1(e) after sampling and interpolation are clearer, without interference, and have good recognizability. Fig. 1(f) is a schematic diagram of the formation of secondary moiré. Assuming that the moiré fringe with frequency f_1 is a cosine wave with intensity I_1, on selecting a point in it at a certain frequency f_2, we can get a new I_3. Then,

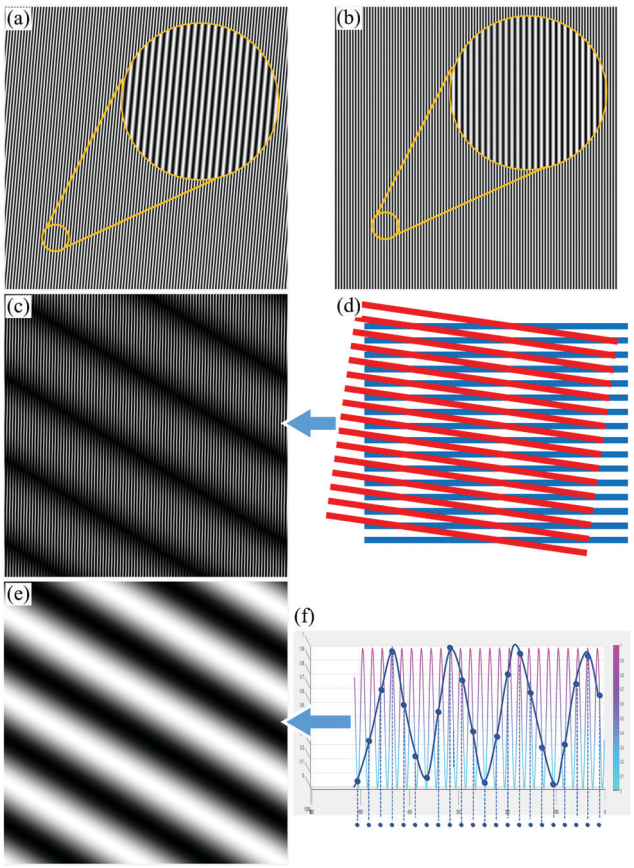

Fig. 1 Formation of the secondary moiré. (a) Schematic diagram of primary moiré fringe. (b) Reference fringe. (c) Moiré fringes formed by geometric superposition. (d) The formation principle of geometric superposition. (e) Moiré fringes formed by digital sampling. (f) The formation principle of digital sampling.

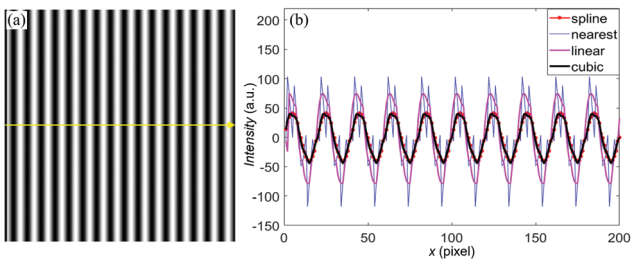

Fig. 2 Secondary moiré obtained by different interpolation sampling (a) the secondary moiré. (b) The sampling error of different interpolation methods.

the cosine wave I_3 is converted into a two-dimensional pattern, as shown in Fig. 1(e), and the obtained moiré fringe pattern will become clearer without changing the internal rules, which is equivalent to re-magnifying the internal information or defects inside the crystal. The second moiré fringe obtained by the sampling fringe method has more advantages when calculating the deformation, and it is faster and more convenient. In contrast, the secondary moiré calculation with geometric

superposition is inconvenient but its formation is simple and fast. More importantly, this method studies the direction, spacing, and angle of moiré fringe formation.

2.2 Calculation of secondary moiré pattern

For a certain secondary moiré pattern, assume that the spacings between the two fringes are p_1 and p_2, and their corresponding frequencies are $f_1 = 1/p_1$ and $f_2 = 1/p_2$. To facilitate analysis, the transmitted light intensity function of the primary moiré fringe and reference fringe can be written as

$$\begin{cases} I_1 = I_a + I_b \cos 2\pi f_1 (\sin \alpha x - \cos \alpha x) \\ I_2 = I_a + I_b \cos 2\pi f_2 x \end{cases} \quad (1)$$

where α represents the angle between the moiré fringe and the horizontal direction; $I_a(x, y)$ and $I_b(x, y)$ are the light intensity of the background and the fringe amplitude, respectively. After the two fringes are superimposed, if a plane wave with intensity I_0 passes through the two fringes continuously, it results in a secondary moiré with the intensity distribution of:

$$\begin{aligned} I &= I_0 I_1 I_2 = I_0 (I_a^2 + I_a I_b \cos 2\pi f_1 (\sin \alpha x - \cos \alpha x) \\ &+ I_a I_b \cos 2\pi f_2 x + I_b^2 \cos 2\pi f_1 (\sin \alpha x - \cos \alpha x) \cos 2\pi f_2 x) \\ &\approx I_0 [I_a^2 + I_a I_b \cos 2\pi f_1 (\sin \alpha x - \cos \alpha x) + I_a I_b \cos 2\pi f_2 x \\ &+ \frac{1}{2} I_b^2 \cos 2\pi (f_1 \sin \alpha x - f_1 \cos \alpha x - f_2 x)] \end{aligned} \quad (2)$$

On the basis of the formation of the secondary moiré, the range of angle and frequency shall meet $-30^\circ \le \alpha \le 30^\circ$, $\frac{2}{3} f_1 \le f_2 \le 2 f_1$.[15]

The calculation of the secondary moiré is obtained by the sampling moiré method. It moves the position of the sampling point along the main direction of the moiré fringes, and performs sampling interpolation in the same way to obtain the phase-shifted secondary sampling moiré. For each moving unit pixel of the sampling point, the shifted phase of the secondary moiré is $2\pi/p_s$, which means that the number of secondary moiré steps of phase-shifting sampling is p_s. Combining the secondary sampling moiré frequency as the difference between the sampling frequency and the primary moiré fringe frequency, *i.e.*, $1/p_m = 1/p_g - 1/p_s$, we can obtain:[21,22]

$$\begin{aligned} I_m(x, y, i) &= I_b(x, y) + I_a(x, y) \\ &\times \cos\left(2\pi x \left(\frac{1}{p_g} - \frac{1}{p_s}\right) + \varphi_0(x, y) + \frac{2\pi i}{p_s}\right) \\ &= I_b(x, y) + I_a(x, y) \\ &\times \cos\left(\varphi_m(x, y) + \frac{2\pi i}{p_s}\right) (i = 0, 1, 2, \ldots, p_s - 1) \end{aligned} \quad (3)$$

where p_g is the period of the moiré fringe (*i.e.*, moiré fringe pitch); $\varphi_0(x, y)$ is the initial phase; i is the first amplitude of the phase-shifted secondary moiré image; φ_m is the secondary moiré phase without phase-shifting.

From the geometric superposition and digital sampling secondary moiré intensity eqn (2) and (3), it can see that in addition to the difference frequency term, eqn (2) also contains the primary moiré intensity not included in eqn (3). This just verifies the difference between the two methods in Fig. 1. The fringes obtained by digital sampling are clearer, purer, and free of interference.

According to the number of phase-shifting steps and the amount of phase-shifting per step, there are many phase-shift algorithms. Here, we adopt the 4-step phase-shifting method to calculate the moiré phase.

$$\varphi_m(x, y) = -\arctan \frac{\sum_{i=0}^{p_s-1} I_m(x, y, i) \sin\left(\frac{2\pi i}{p_s}\right)}{\sum_{i=0}^{p_s-1} I_m(x, y, i) \cos\left(\frac{2\pi i}{p_s}\right)}, \quad (i = 0, 1, 2, 3) \quad (4)$$

It can be seen from eqn (4) that the moiré phase is obtained by the arctangent function, and the value range is $(-\pi, \pi]$. If the moiré phase exceeds this range, it will be wrapped in $(-\pi, \pi]$, resulting in jump points in the phase map. Therefore, it is necessary to carry out phase unwrapping ($\pm 2n\pi$ at the jump points) to eliminate the phase jump points so that the phase field changes continuously, and finally the unwrapped phase-field φ_m can be obtained.

Then, the displacement field according to the relationship between the phase difference before and after the deformation is achieved by:

$$u_x(x, y) = \frac{p_g(\varphi_m(x, y) - \varphi_m'(x, y))}{2\pi} = \frac{p \Delta \varphi_m(x, y)}{2\pi} \quad (5)$$

where φ_m' is the phase field of the unwrapped moiré after the deformation.

Therefore, the strain fields of the secondary nano-moiré can be deduced as:[23]

$$\begin{cases} \varepsilon_x = \dfrac{\partial U}{\partial x} = \dfrac{p}{2\pi} \dfrac{\partial \Delta \varphi_m(x, y)}{\partial x} \\ \varepsilon_y = \dfrac{\partial V}{\partial y} = \dfrac{p}{2\pi} \dfrac{\partial \Delta \varphi_n(x, y)}{\partial y} \\ \gamma_{xy} = \dfrac{\partial U}{\partial y} + \dfrac{\partial V}{\partial x} = \dfrac{p}{2\pi} \left(\dfrac{\partial \Delta \varphi_m(x, y)}{\partial y} + \dfrac{\partial \Delta \varphi_n(x, y)}{\partial x} \right) \end{cases} \quad (6)$$

Eqn (6) is applicable to strain calculation in a large deformation area, *i.e.*, when the phase can be calculated, the real strain field can be obtained by subtracting the undeformed carrier. However, if the deformation area is relatively small and there are large undeformed areas in the map, the deformed primary moiré can be sampled at a similar frequency to obtain the deformed secondary moiré. At this time, the pattern contains not only the secondary moiré information of the initial carrier generated by the mismatch between the moiré and the reference fringe but also the secondary moiré after deformation. The real strain can be obtained by subtracting the deformed moiré fringe with the initial carrier moiré fringe formed in the

undeformed area, which is expressed as:

$$\begin{cases} \varepsilon_x^{\mathrm{d}} = \varepsilon_x^1 - \varepsilon_x^0 = \left(\dfrac{\Delta m_{\mathrm{u}}^1}{\Delta x^1} - \dfrac{\Delta m_{\mathrm{u}}^0}{\Delta x^0}\right) p_{\mathrm{r}} \\ \varepsilon_y^{\mathrm{d}} = \varepsilon_y^1 - \varepsilon_y^0 = \left(\dfrac{\Delta m_{\mathrm{v}}^1}{\Delta x^1} - \dfrac{\Delta m_{\mathrm{v}}^0}{\Delta x^0}\right) p_{\mathrm{r}} \end{cases} \quad (7)$$

where superscripts 0 and 1 respectively represent the deformed secondary fringe and the initial carrier constructed from the undeformed area.

The core of secondary sampling moiré measurement is to analyze the deformation information of the carrier through the deformation grating. Traditional methods mostly use the form of fringe as the measurement structure. The digital phase-shifting technique is a fringe automatic analysis technology, which can further improve the accuracy of the calculation. There is no need to determine the sign of the fringe. The results obtained by the solution is the phase value of each point on the fringe pattern. Here, we move the collected initial phase position through a computer program, which is equivalent to moving the reference grating. Furthermore, the advantage of sequential digital phase-shifting is that it can easily achieve phase-shifting without the optical devices.

The secondary sampling moiré method combines the moiré method with computer processing technology. Based on a single grating image, a moiré image is formed through sampling and interpolation, and moiré phase-shifting is achieved by moving the sampling point. The phase analysis and deformation calculation of the moiré can be completed without superimposing the reference grating and experimental phase-shifting hardware. It can realize the digitization and automation of grating deformation measurement, improve the measurement efficiency, and flexibly adjust the sampling frequency and sampling direction to meet different measurement requirements.

In the actual sampling to obtain the secondary moiré, interpolation is required to get an image with the same size as that of the original image. Here, we explore the influence of different interpolation functions on the results. Fig. 2(a) shows the secondary moiré pattern obtained by different interpolation sampling. When sampling to generate the pattern, the original pixel image cannot be directly obtained, so interpolation is required. The commonly used method is the nearest interpolation, which is the fastest, but the smoothness of the data is the worst, and the changes are generally discontinuous. The bilinear interpolation algorithm ('linear'), compared with the above, occupies more memory and the execution speed is slightly slower, but the data smoothness is better, and the data is continuously changing. The cubic spline interpolation ('spline') has the slowest speed, small memory usage, and smooth data. Bi-cubic interpolation ('cubic') is worse than linear in terms of speed and memory, but the data and the first derivative are continuous. Using the above four different interpolation methods, the difference between the calculated and theoretical sine function is shown in Fig. 2(b). It can be seen that for a sine wave, the error distributions of the nearest interpolation and bilinear interpolation are relatively large; thus, they are not considered in this work.

2.3 Simulation analysis

In order to obtain the accuracy of the strain field measured by the secondary moiré method, the strain field of a theoretical lattice with the center stretched to the surroundings was analyzed, as shown in Fig. 3.

Fig. 3(a) shows the theoretical strain field, where the center was stretched, and the surroundings were compressed expansion. Fig. 3(b) is the dense deformed primary moiré fringe in the x-direction generated by the strain field in Fig. 3(a). After geometric superposition and secondary sampling, and four-step phase-shifting, Fig. 3(c) and (d) are obtained. Fig. 3(e) is the strain field of the geometrically superimposed moiré obtained by Fig. 3(c). It can be seen that due to the interference of the primary moiré, the strain field has a lot of fringe interference. Fig. 3(f) is the strain field calculated by Fig. 3(d). The advantage of the secondary moiré is that the original deformation can be further enlarged to obtain the deformed fringes visible to the naked eye, which makes the observation more intuitive and convenient. Moreover, in an ordinary TEM experiment, the field of view for observation can be further expanded without changing the accuracy of the measurement. Here, the digital phase-shifting was performed on secondary moiré fringes to obtain four secondary moiré patterns with a difference of $\pi/2$. Then, the strain field was calculated by eqn (7), as shown in Fig. 3(f). At the same position in the middle of the y-axis of the strain fields obtained by the above two methods, cross sections from Fig. 3(e and f) along the x-direction were selected to compare the strain values, as shown in Fig. 3(g). It can be seen that the trend of the results is consistent. The strain value calculated by the geometric superposition of the secondary moiré method has a certain ringing effect, while the result of the sampling secondary moiré does not. Comparing the middle-scribed part of the strain with the

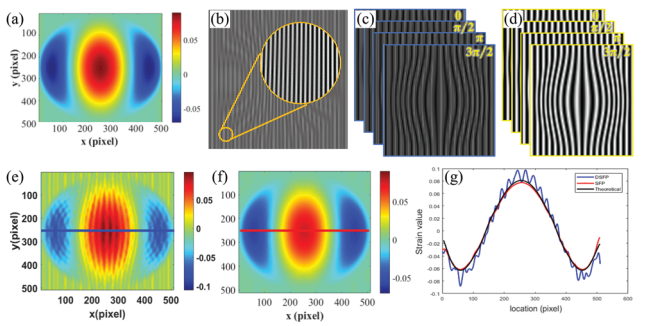

Fig. 3 Simulated deformation of a theoretical lattice. (a) Theoretical strain field; (b) generation of the primary moiré in the x-direction; (c) the secondary moiré in the x-direction obtained by geometric superposition with four-step phase-shift was carried out; (d) the secondary moiré in the x-direction obtained by sampling with four-step phase-shift was carried out; (e) the strain field calculated by the geometric superposition of secondary moiré and phase-shifting; (f) the strain field calculated by sampling secondary moiré and phase-shifting; (g) the strain values of the scribed parts in (a), (e), and (f).

theoretical value, it is found that the sampling secondary moiré error is 4.12%, which is closer to the real strain.

3. Results and discussion

In this study, the sampling secondary moiré method was used to measure the strain field at the interface of Si/Ge heterostructure (often used in heterojunction bipolar transistors), as shown in Fig. 4. In the experiment, the STEM used was a Fei Titan Themis200 with spherical aberration correction. The voltage was set as 200 kV, and the half convergence angle of the electron beam α was 17.9 mrad. When characterizing the strain field of semiconductors on the nanoscale, high sensitivity and a large field of view are required.

The substrate material of the heterostructure is Si(200), on which germanium was grown by molecular beam epitaxy, and then it made into the interface samples, as shown in Fig. 4(a). It can be seen that the growth direction of Si was [011], and then 300 nm Ge with the same crystal direction was deposited on it. The sample was prepared by a Focused Ion Beam instrument (FIB, FEI Helios Nanolab 450S). Fig. 4(b) shows the BF-STEM atomic structure at the interface of the Si/Ge heterostructure in the STEM mode. After a certain magnification, it can be seen that there are three edge dislocations at the interface. Fig. 4(d) shows the primary moiré fringes obtained in the STEM mode. The formation is a result of the interference between the Si(11$\bar{1}$), Ge(11$\bar{1}$), and the scanning line. The field of view obtained in this way is at least ten times larger than that of the atomic image, but the moiré information in it needs to be magnified many times to see clearly. After sampling it at a similar frequency, the secondary parallel moiré shown in Fig. 4(e) can be obtained. It is obvious that the moiré on both sides of the interface has different frequencies; thus, the position of the interface can be roughly estimated. To determine the position of the interface more accurately, the digital secondary geometric superposition moiré can be used. The advantage is that the moiré and its formation law can be easily obtained by direct superposition. Compared with the sampling secondary moiré, this method does not require interpolation, and can be used to study the formation of complex graphics after superposition, such as the regular distributions of binarization 0, 1 interval fringes and regular polygons. Here, we used it to form Fig. 4(f). It can be seen that the secondary moiré on both sides of the interface deflects in different directions. Connecting the ends of the deflection lines close to the interface is the real Si/Ge interface. In order to pursue sufficient accuracy, the superimposed fringes with similar frequencies can be rotated to a specific angle so that the deflected fringes in the visual plane are dense enough and there are enough endpoints at the connection interface.

The strain field at the Si/Ge interface was then calculated. Fig. 5(a) shows the bright field moiré pattern at the interface of the Si/Ge heterostructure in the STEM mode, with the scanning spacing of 0.27 nm. Similarly, after Fourier transformation, the excess noise was filtered out, and the useful moiré fringe information was extracted (here, partial fringes in the red area were extracted). After secondary sampling and digital phase-shifting processed, Fig. 5(b) was obtained. The phase map was obtained by 4-step phase-shifting and unwrapping. The phase of the reference region was subtracted to obtain the true deformation phase map, and then the real strain field components $\varepsilon_{11\bar{1}}$ at the interface were calculated, as shown in Fig. 5(d). Fig. 5(e) shows the BF-STEM double PMMF[24] of the Si/Ge heterostructure with a scanning spacing of 0.75 nm. The field of view is 776 × 776 nm^2, which is 7.68 times larger than that of the natural moiré in Fig. 5(a). Similarly, the moiré fringes in the red area in Fig. 5(e) underwent a series of processes to obtain Fig. 5(f). It can be seen that there are six mismatched dislocations in Fig. 5(d) that are periodically distributed at the interface, which is caused by the lattice mismatch of silicon and germanium. The measured periodic length of adjacent

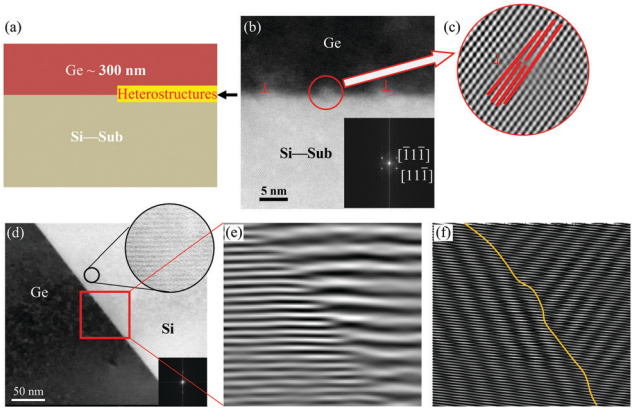

Fig. 4 Interface recognition based on secondary moiré. (a) Schematic diagram of the Si/Ge material. (b) Atomic structure of Si/Ge at the interface; (c) enlarged view of the interface atomic structure in the red area of (b); (d) STEM moiré fringe patterns at the interface of an Si/Ge heterostructure; (f) parallel moiré of secondary sampling. (g) Corner moiré of secondary geometric superposition.

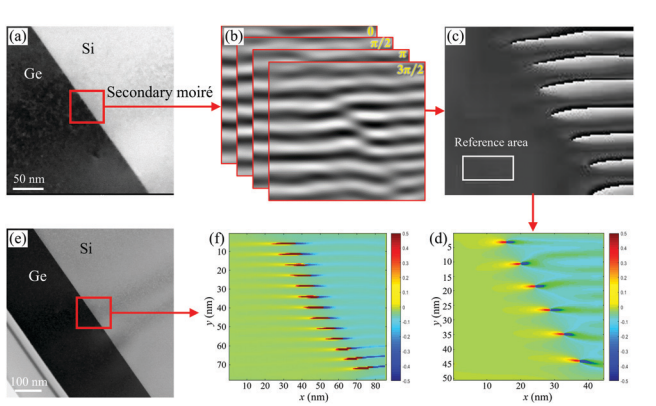

Fig. 5 Calculation of strain field: (a) STEM bright-field moiré fringe patterns at the interface of the Si/Ge heterostructure; (b) secondary sampling moiré; (c) unwrapping phase; (d) real strain field components $\varepsilon_{11\bar{1}}$ at the interface with the dislocation; (e) double multiplication moiré fringe patterns at the interface of the Si/Ge heterostructure; (f) the strain field calculated from the red area in (a).

dislocations is 9.64 nm, which is consistent with the classical Matthews-Blakeslee (MB) model.[25]

For heterostructures, the misfit strains caused by the interfacial mismatch accumulates with the increase in the epitaxial thickness. When the thickness of the epitaxial layer reaches a certain critical value h_c, a mismatch dislocation will be generated at the interface of the heterostructures to release the accumulated strain, which is belonging to the dislocation system $\{111\}\langle 110\rangle$.

The in-plane growth is carried out by adsorbing atoms at the edge of the step and making the step migrate on the growth surface. Generally, the unstressed lattice size a_f of the thin film material parallel to the interface is different from the lattice size a_s of the substrate, and the difference can be as high as several percentage points. However, the atoms of the film material will be arranged according to the position of the base atoms and continue its atomic structure. At this time, the film material will bear the necessary strain at the interface to make the growth possible. The mismatch strain caused by the mismatch of the lattice parameters is $\varepsilon_m = (a_s - a_f)/a_s$. Fig. 4(b) shows a cross-sectional view of the heterostructure interface. The lattice mismatch between the film and the substrate is large, and both have a diamond structure. In this case, the mismatch strain is about 4.18%. However, the lattice mismatch in the film is caused by the relaxation of the elastic strains, which resulted in the formation of very regularly arranged interface misfit dislocations. Each dislocation has its own Burgers vector on the interface. If this is the case, there will be an edge dislocation caused by the lattice mismatch every 9.6 nm, which can be calculated from the actual (011) direction lattice spacing in the plane, and is consistent with the experimental observations. It can be seen from Fig. 5(a) and (e) that the dislocations at the Si/Ge interface are arranged periodically. By calculating the distance between the dislocations, it was found that the position of the dislocations was closely related to the misfit degree of crystal growth. In other words, when the material at the interface accumulates to a certain extent, the elastic stress caused by the mismatch will be released in the form of dislocation, thus forming a periodic edge dislocation. The results show that more dislocations and larger measurement areas can be seen when the field of view is increased.

Fig. 6 shows the strain field of dislocation in the x-direction at the interface of Si/Ge heterostructure, of which Fig. 6(a) is the experimental result, and Fig. 6(b) is the strain field of the Peierls Nabarro (P–N) dislocation model. In this model, the strain of edge dislocation along the x-direction can be expressed as

$$\varepsilon_{xx} = \frac{b}{\pi}\frac{(1-\nu)y}{4(1-\nu)^2x^2 + y^2} \tag{8}$$

where x and y are respectively the right-angle coordinates centered on the dislocation core position, b is Burgers vector, and ν is the Poisson's ratio. In the Foreman dislocation model, the strain of edge dislocation along the x-direction can be

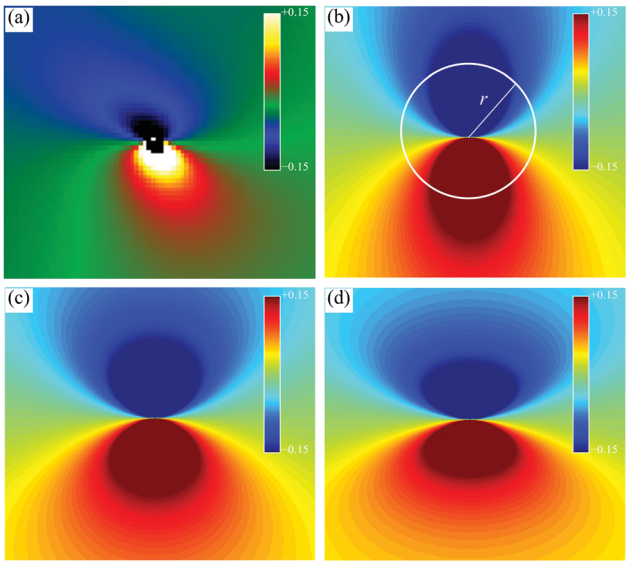

Fig. 6 The strain field of a dislocation in the x-direction at the interface of the Si/Ge heterostructure: (a) experimental strain field. (b) Strain field of the P–N dislocation model. (c)–(f) The Foreman dislocation model strain fields shown with a = 2 and 3, respectively.

expressed as

$$\varepsilon_{xx} = \frac{b(1-\nu)}{\pi}\frac{4(1-\nu)^2yx^2 + 2(a^3 - a^2)y^3}{\left[4(1-\nu)^2x^2 + a^2y^2\right]^2} \tag{9}$$

where a is the alterable factor that can control the dislocation width. Fig. 6(c) and (d) are the Foreman dislocation model strain fields with a = 2 and 3, respectively.

In order to make a more precise comparison, we drew a circle with a radius of 5 pixel with the core of the dislocation as the center. The abscissa is the angular degree and the ordinate is the value of the dislocation, as shown in Fig. 7. By comparing

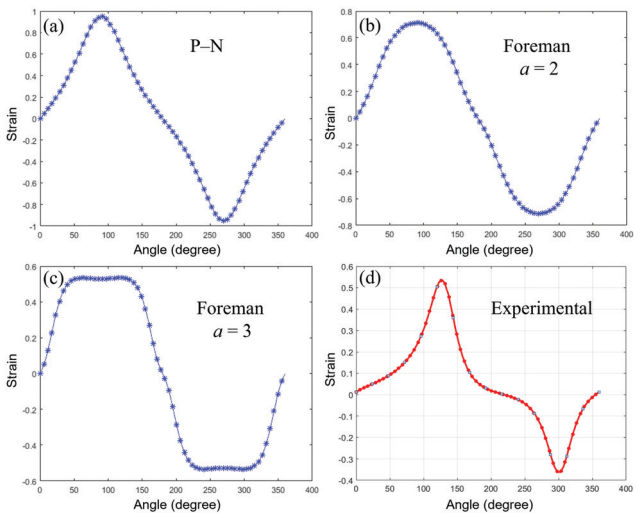

Fig. 7 Strain distribution of different models and experiments: (a) P–N dislocation model; (b) and (c) the Foreman dislocation model with a = 2 and 3, respectively; (d) dislocations of experimental results.

the theoretical value and the experimental data, it is found that the dislocation result curve of Fig. 7(d) in this experiment is closer to the theoretical strain field of the P–N dislocation model shown in Fig. 7(a).

4. Conclusions

In the field of micro-/nano-electronic technology, strained silicon and strain engineering are widely used. Phenomena such as interface mismatch strain and residual strain/stress can be seen everywhere. When using scanning moiré to characterize the strain field, the fringes are often too dense to be directly observed. This is because in the existing two-dimensional STEM moiré technology, the scanning line and magnification of the TEM cannot be changed continuously. The lattice spacing is usually difficult to match with the fixed scan spacing, making most of the generated fringes too dense. In this paper, the STEM secondary nano-moiré method was proposed and its formation principle was analyzed. There are two ways to form the secondary moiré, *i.e.*, sampling and geometric superposition. Among them, the sampling secondary moiré can automatically analyze and process the original fringes, while the phase-shifting technique can improve the accuracy of calculation and make the measurement of strain field automatic and digitized. The advantage of secondary moiré formed by geometric superposition is that it is simple and can quickly obtain the moiré at any angle. Studying its formation law is helpful to accurately determine the interface position. The simulation experiment shows that the sampling secondary moiré method has a smaller error than the geometric superposition method. The experimental measurement of the misfit strain of the Si/Ge interface shows that the geometric superposition secondary moiré method can quickly find the interface position, while the sampling secondary moiré can be used to calculate the interface misfit strain. In the strain field calculated by the sampling secondary moiré, the dislocations on the Si/Ge interface are arranged periodically. By calculating the period of dislocation, it is found that the dislocation location is closely related to the degree of mismatch of crystal growth. Comparing the experimentally measured single dislocation with the theoretical model, it can be seen that they are consistent with the P–N dislocation model. The STEM secondary nano-moiré method proposed in this work is suitable for a wide range of nanostructures' analysis.

Author contributions

Yao Zhao: conceptualization, methodology, formal analysis, writing – original draft; Zhanwei Liu: visualization, writing review & editing; Xianfu Huang: validation, writing review & editing; Yang Yang, Huihui Wen: resources, data curation; Chao Liu: supervision, editing.

Conflicts of interest

There are no conflicts to declare.

Acknowledgements

This work was financially supported by the National Natura Science Foundation of China (11972084), National Science and Technology Major Project (2017-V1-0003-0073), Beijing Natural Science Foundation (1192014).

Notes and references

1 J. C. Bean, *Proc. IEEE*, 1992, **80**(4), 571–587.
2 Z. I. Alferov, *Semiconductors*, 1998, **32**, 1–14.
3 J. P. Hill, Y. Wakayama and K. Ariga, *Phys. Chem. Chem. Phys.*, 2006, **8**, 5034–5037.
4 G. I. Tóth, G. Tegze, T. Pusztai and L. Gránásy, *Phys. Rev. Lett.*, 2012, **108**(2), 25502.
5 E. Wood and F. Sansoz, *Nanoscale*, 2012, **4**, 5268–5276.
6 X. Junhua, L. Geyang and G. Mingyuan, *Thin Solid Films*, 2000, **370**, 45–49.
7 K. Ohashi, in *Silicon-Germanium (SiGe) Nanostructures*, ed. Shiraki, Y. and Usami, N., Woodhead Publishing, 2011, pp. 551–574.
8 H. Zhang, H. Wen, Z. Liu, Q. Zhang and H. Xie, *Nanoscale*, 2017, **9**, 15923–15933.
9 T. Boyko, T. Gross, M. Schwarz, H. Fuess and A. Moewes, *J. Mater. Sci.*, 2014, 49.
10 J. Li, C. Zhao, Y. Xing, S. Su and B. Cheng, *Materials*, 2013, **6**, 2130–2142.
11 Q. L. Liu, C. W. Zhao, Y. M. Xing, S. J. Su and B. W. Cheng, *Opt. Laser Eng.*, 2012, **50**, 796–799.
12 H. H. Liu, X. F. Duan and Q. X. Xu, *Micron*, 2009, **40**, 274–278.
13 F. Huee, M. Hyetch, F. Houdellier, H. Bender and A. Claverie, *Appl. Phys. Lett.*, 2009, **95**, 73103.
14 D. Su and Y. Zhu, *Ultramicroscopy*, 2010, **110**, 229–233.
15 S. Kim, S. Lee, Y. Oshima, Y. Kondo, E. Okunishi, N. Endo, J. Jung, G. Byun, S. Lee and K. Lee, *Appl. Phys. Lett.*, 2013, **102**, 161604.
16 H. Wen, H. Zhang, Z. Liu, C. Liu, S. Liu, X. Yang, F. Liu and H. Xie, *Appl. Phys. Lett.*, 2018, **113**, 31905.
17 Y. Wang, J. Bruley, H. Meer, J. Li, A. Domenicucci, C. Murray and J. Rouviere, *Appl. Phys. Lett.*, 2013, 103.
18 S. Kim, Y. Jung, J. Jung Kim, G. Byun, S. Lee and H. Lee, *Appl. Phys. Lett.*, 2014, **104**, 161610.
19 Q. Zhang, H. Xie, Z. Liu and W. Shi, *Opt. Laser Eng.*, 2018, **107**, 315–324.
20 Q. Wang, S. Ri and H. Tsuda, *Appl. Opt.*, 2016, **55**, 6858–6865.
21 S. Ri, M. Fujigaki and Y. Morimoto, *Exp. Mech.*, 2010, **50**, 501508.
22 G. Borgefors, I. Amidror, R. Deriche, T. S. Huang, K. Ikeuchi, T. Jiang, R. Klette, A. Leonardis, H. Peitgen and J. K. Tsotsos, *The Theory of the Moire Phenomenon*, Springer, London, 2009.
23 D. Fulong, S. Guanlin and X. Huimin, *Experimental mechanics*, Tsinghua University Press, 2010.
24 Y. Zhao, D. Wu, J. Zhou, H. Wen, Z. Liu, Q. Wang and C. Liu, *Nanotechnology*, 2021, **32**, 475705.
25 A. Braun, K. M. Briggs and P. Boni, *J. Cryst. Growth*, 2002, **241**, 231–234.

